Front. Energy 2024, 18(3): 390–398
https://doi.org/10.1007/s11708-023-0901-9

RESEARCH ARTICLE

**Junwen CAO, Yun ZHENG, Wenqiang ZHANG, Bo YU**

# Plasma spray coating on interconnector toward promoted solid oxide fuel cells and solid oxide electrolysis cells



**Abstract** Interconnector is a critical component to construct solid oxide cells (SOCs) stack. Oxidation of metallic interconnectors and Cr poisoning caused by oxidation are important factors that lead to long-term performance degradation of SOCs. Coating on the interconnector surface is an important approach to inhibit the oxidation and Cr migration of the interconnector. Herein, $(La_{0.75}Sr_{0.25})_{0.95}MnO_{3-\delta}$ (LSM) and $Mn_{1.5}Co_{1.5}O_4$ (MCO) are used to fabricate the coatings of interconnector. Two advanced thermal spray technology, atmospheric plasma spraying (APS) and low-pressure plasma spray (LPPS), are adopted for the coating preparation. The electrochemical performance, rising and cooling cycle stability, and Cr diffusion inhibition performance of the coatings are tested and evaluated. The result indicates that MCO can generate more uniform and denser coatings than LSM. In addition, MCO coatings prepared by LPPS shows the best electrochemical performance, rising and cooling cycle stability, and Cr diffusion inhibition. The initial area specific resistance (ASR) is 0.0027 $\Omega \cdot cm^2$ at 800 °C. After 4 cooling cycle tests, the ASR increases to 0.0032 $\Omega \cdot cm^2$ but lower than other samples. Meanwhile, the relative intense of Cr at the interface of SUS430 with MCO coatings fabricated by LPPS is lower than that of MCO fabricated by APS after 4 rising and cooling cycle operations, showing more favorable Cr diffusion inhibition performance.

Received Aug. 16, 2023; accepted Sept. 21, 2023; online Nov. 10, 2023

Junwen CAO, Wenqiang ZHANG, Bo YU (✉)
Institute of Nuclear and New Energy Technology (INET), Collaborative Innovation Center of Advanced Nuclear Energy Technology, Tsinghua University, Beijing 100084, China
E-mail: cassy_yu@mail.tsinghua.edu.cn

Yun ZHENG
Department of Chemical Engineering, University of Waterloo, Waterloo, Ontario N2L 3G1, Canada; Institute of New Energy Materials and Engineering, School of Materials Science and Engineering, Fuzhou University, Fuzhou 350108, China

Special Issue: Electrochemical Energy Storage and Conversion of Hydrogen Energy

**Keywords** interconnector coating, plasma spray, electrochemical performance, Cr diffusion inhibition, solid oxide cells (SOCs)

## 1 Introduction

Solid oxide cells (SOCs) have attracted global attention due to their high energy conversion efficiency, low pollution emission, relatively flexible fuel choice, and the capability to meet the requirement for large scale energy storage and conversion [1–3]. SOCs have two reversible operating models, solid oxide fuel cell (SOFC) and solid oxide electrolysis cell (SOEC). SOFC can convert chemical fuels, such as $H_2$, CO, and hydrocarbons, directly to electricity with high energy efficiency, high energy and power densities [4–6]. In contrast, SOEC can store electricity into chemical fuels, such as $H_2$, CO, or syngas, through water electrolysis, $CO_2$ electrolysis or $H_2O/CO_2$ co-electrolysis [7,8]. Due to the above characteristics, SOCs are considered as a robust and flexible energy conversion technology to cope with the wide range of operating conditions in future energy scenarios. Historically, long-term stability and thermal (cool-down/heat-up) and emergency shutdown cycle tolerance have posed critical challenges to multi-scenario applications of SOCs [1].

Interconnector is a critical component in SOC stacks, which provides electrical connection between contiguous cells as well as separation of oxygen (cathode side in SOFC model) and fuel gases and/or steam (anode side in SOFC model) [9–11]. Fe–Cr based metallic materials, such as Crofer22 APU, SUS304, and SUS430, have been widely used in the interconnector of SOCs due to their excellent electrical conductivity, high-temperature structural stability, and matched coefficient of thermal expansion (CTE) with other SOC components [12–14]. However, $Cr_2O_3$ scale, which is formed by oxidation of interconnector at a high temperature, is known to cause performance degradation of the stacks [15–17].

Furthermore, $Cr_2O_3$ can react with $O_2$ and $H_2O$ to form $CrO_3$ or $CrO_2(OH)_2$ to poison the cathode of SOFC (anode of SOEC) and further deteriorate SOC performance [18–20]. These two negative factors lead to poor long-term stability and thermal (cool-down/heat-up) cycle tolerance of SOCs.

Coating a conductive ceramic layer on interconnector is an effective method to inhibit the growth rate of $Cr_2O_3$ scale and prevent the diffusion of $CrO_3$ or $CrO_2(OH)_2$ [21–23]. A lot of ceramic materials including oxides, perovskites ($La_{1-x}Sr_xMnO_3$ [24]) and spinels ($Mn_xCo_{3-x}O_4$ [25,26], $Cu_xFe_{3-x}O_4$ [27,28], $Ni_xFe_{3-x}O_4$ [29,30], etc.) have been used as the coatings of interconnector. Screen printing, sol-gel, magnetron sputtering [31] and plasma spraying [32], electrophoretic deposition [33,34] and so on are used to the coating preparation. However, as an important index to evaluate the long-term stability and durability of SOC coatings, there are few studies on rising and cooling cycle test.

In this study, $(La_{0.75}Sr_{0.25})_{0.95}MnO_{3-\delta}$ (LSM) and $Mn_{1.5}Co_{1.5}O_4$ (MCO) powders are applied to the preparation of interconnector coatings. To meeting the needs of higher requirement of coating uniformity and large-scale coating fabrication, two thermal spraying technologies, atmospheric plasma spraying (APS) and low-pressure plasma spray (LPPS), are used for the coating preparation. The structure, morphology, and electrochemical performance of different coatings fabricated using different methods are investigated and compared in detail. Cr diffusion-inhibited performance of the MCO coatings is tested and evaluated on rising and cooling cycle operation.

## 2 Experimental

### 2.1 Powder characterization and granulation

The LSM and MCO powders used to fabricate coatings in this study were purchased from Ningbo SOFCMAN Energy Technology Co., Ltd. and Fuelcell Energy, Inc., respectively. X-ray diffraction (XRD, Cu Kα radiation) was used to confirm the crystal patterns and the four-electrode method was used to measure the electrical conductivity of the two powders. The median particle size ($d_{50}$) of the powder in the thermal spraying process must be greater than 25 μm. However, the $d_{50}$ of the initial LSM and MCO are 0.5–2 μm and 0.5–0.84 μm, respectively, which cannot meet the requirements of thermal plasma spraying process. Therefore, spray drying granulation process [35] was adopted to prepare suitable particle size powder before plasma spraying, and scanning electron microscopy (SEM) was adopted to characterize the morphology and particle size of the powders after granulation.

### 2.2 Interconnector coating preparation by plasma spraying process

LSM and MCO coatings were prepared on stainless steel (SUS430) interconnector. The two kinds of coatings (LSM-APS and MCO-APS) were manufactured by APS in the Oerlikon Metco UniCoat F4 system. In addition, the MCO coating was also manufactured by LPPS in the Sulzer Metco LPPS-TF system (MCO-LPPS).

The spraying process schematic was shown in Fig. 1. For the APS process, SUS430 substrates were mounted on fixture, and the granulation powders were transported to the plasma torch by carrier gas. Then, a mechanical arm moved torch along a path and the powders were sprayed by the torch to coat stationary substrates at a standoff distance. Different from APS, LPPS need to be vacuumed and maintained in an inert gas state during the spraying process. After SUS430 substrates were mounted on fixture, the LPPS system was vacuumed and filled with inert gas. Then, a spraying process similar to APS was operated. Air was not allowed into the LPPS system until the substrates were sprayed and cooled to room temperature. The SUS430 samples of 10 mm × 10 mm × 2 mm were sprayed on both sides. The operating parameters of the two plasma spraying processes are listed in Tables 1 and 2, respectively. The surficial and cross-section morphologies and structures of the rectangular samples with different coatings were observed using SEM, and the distribution of characteristic elements of the samples at the interface was detected and analyzed using energy dispersive spectrometer (EDS) in linear scan mode.

### 2.3 Electrochemical measurement

As shown in Fig. 2, the electrical resistance of the rectangular samples was measured by using a four-point method from 650 to 800 °C in air, and interconnector samples without coating were used as comparisons. Ag

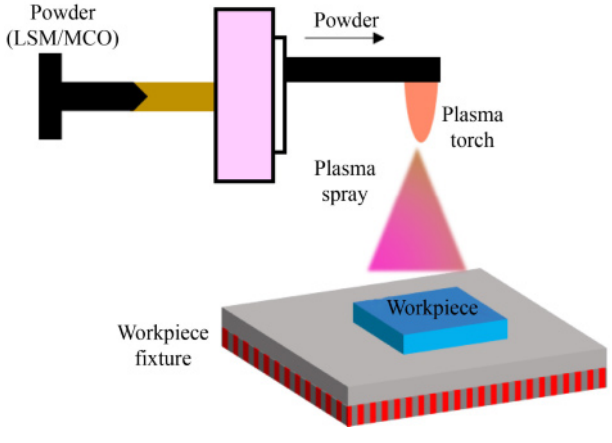


**Fig. 1** Schematic of spraying process for coating spray.

**Table 1** Main parameters of APS process

| Parameter | Value |
|---|---|
| Power/kW | 48 |
| Torch current/A | 515 |
| Flow rate of Ar/(L·min$^{-1}$) | 40 |
| Flow rate of $H_2$/(L·min$^{-1}$) | 12 |
| Standoff distance/mm | 110 |
| Powder feed rate/(g·min$^{-1}$) | ~10 |
| Rotational speed/% | 15 |
| Stirring rate/% | 60 |
| Cooling gas/MPa | 0.15 |

**Table 2** Main parameters of LPPS process

| Parameter | Value |
|---|---|
| Vacuum chamber pressure/Pa | 50 |
| Power/kW | 115 |
| Plasma current/A | 2200 |
| Flow rate of Ar/(L·min$^{-1}$) | 80 |
| Flow rate of He/(L·min$^{-1}$) | 90 |
| Standoff distance/mm | 650 |
| Powder feed rate/(g·min$^{-1}$) | 80 |
| Powder gas flow rate (Ar, L·min$^{-1}$) | 10 |
| Spraying line velocity/(mm·s$^{-1}$) | 300 |
| Preheating temperature/°C | 700 |
| Cooling pressure/MPa | 50 |
| Cooling time/min | 20 |

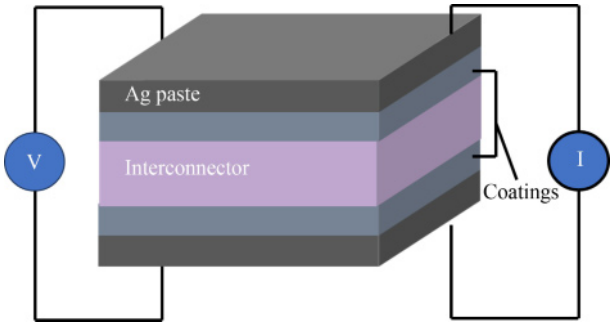


**Fig. 2** Schematic of ASR measurement setup.

paste was used as current collector in the electrochemical measurement. The resistance ($R$) of the samples was measured using an electrochemical workstation (IM6ex, Zanher) in the mode of electrochemical impedance spectroscopy (EIS) with an amplitude of applied voltage of 10 mV and a frequency range of 1 MHz to 0.1 Hz. The area specific resistance (ASR) was calculated using

$$\mathrm{ASR} = \frac{R \times A}{2}, \quad (1)$$

where $A$ is the superficial area of the rectangular samples. The stability and durability of the coatings were evaluated by several rising and cooling cycle tests from room temperature to 800 °C. After electrochemical test, the cross-section patterns of the samples were observed using SEM and the Cr diffusion phenomenon at the interface was detected and evaluated using EDS.

## 3 Results and discussion

### 3.1 Structure, morphology, and performance of LSM and MCO powder

The structure, morphology, and basic performance of the LSM and MCO powders are measured and analyzed to provide reference for the preparation and performance analysis of corresponding coatings. Crystal structures of the initial LSM and MCO powders are identified by XRD patterns in Figs. 3(a) and 3(b). LSM (PDF#89-4461) shows a typical perovskite crystal type while MCO (PDF#84-0482) shows a typical spinel crystal type, and no impurity phase is detected within the two powders. The diffraction pattern for the LSM powder has 8 peaks at 22.9°, 32.5°, 40.2°, 46.8°, 52.6°, 58.0°, 68.1°, and 78.0°, corresponding to (012), (110), (202), (024), (122), (300), (220), and (128), respectively, while that for the MCO powder has 9 peaks at 18.5°, 30.5°, 35.9°, 37.6°, 43.7°, 54.2°, 57.8°, 63.5°, and 76.2°, corresponding to (111), (220), (311), (222), (400), (422), (511), (440), and (622), respectively. The electronic conductivity test results are demonstrated in Fig. 3(c). The electronic conductivity ($\sigma$) of LSM is obviously higher than that of MCO. At 800 °C, which is a general operating temperature of SOCs, for instance, the $\sigma$ of LSM is 155.56 S/cm$^2$, 2.6 times larger than that of MCO.

The SEM patterns of LSM and MCO granulation powders are provided in Figs. 4(a) and 4(b) and Figs. 4(c) and 4(d), respectively. The LSM and MCO powders have a typical spherical particle morphology, as shown in Figs. 4(a) and 4(c). The particle size and uniformity of the powders are measured and analyzed from Fig. 4, which provides a preliminary judgment on whether the corresponding powder is suitable for coating preparation. The homogeneity of LSM, with a diameter ranging from 18.44 to 31.55 μm (measured in Fig. 4(b)), is more uneven than that of MCO with a diameter of approximately 37.9 μm (measured in Fig. 4(d)). As a result, the MCO granulation powder is more suitable for the thermal plasma spraying process due to the more uniform and larger particle morphology.

### 3.2 Structure and morphology of LSM and MCO coatings

The structures and morphologies of the SUS430 samples with different coatings are shown in Fig. 5. As

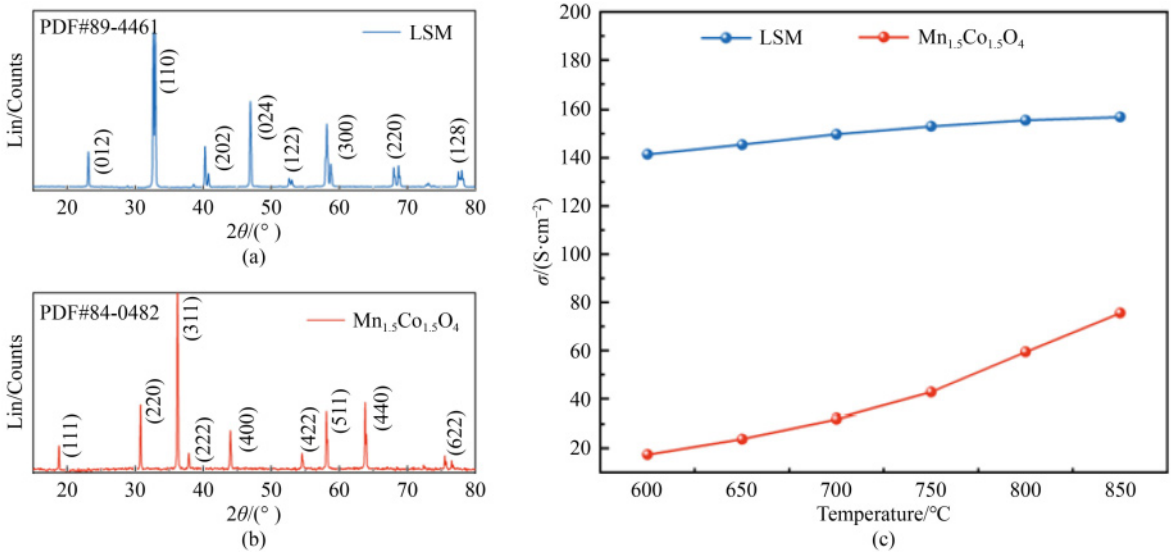


**Fig. 3** Structure and performance of LSM and MCO powders.

(a) XRD patterns of initial LSM (PDF#89-4461); (b) XRD patterns of MCO (PDF#84-0482); (c) electronic conductivity of LSM and MCO at different temperatures.

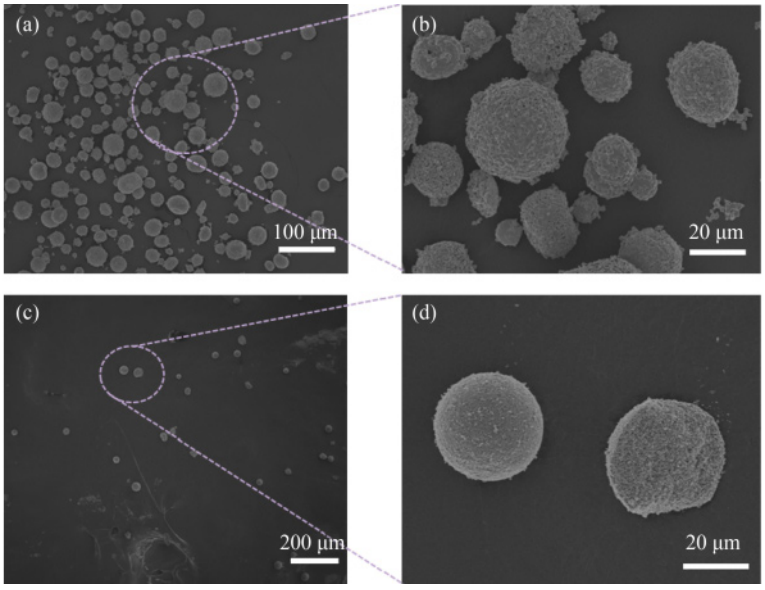


**Fig. 4** Morphology of two powders.

(a) Morphology of LSM granulation powder; (b) locally enlarged image of LSM granulation powder; (c) morphology of MCO granulation powder; (d) locally enlarged image of MCO granulation powder.

demonstrated in Figs. 5(a), 5(d), and 5(g), the surface of SUS430 with different coatings is not obviously spherical particles of powders, but in a flat and dense structure. The locally enlarged images of Figs. 5(a), 5(d), and 5(g) shown in Figs. 5(b), 5(e), and 5(h) reveal that the three coatings are composed of micro/nano-particles and the particles size is smaller than the granulation powder before spraying, suggesting that the sprayed powder undergoes a process of melting and recrystallization, which results in a strong bonding between powders caused by melting, improving the gas barrier capacity of the coatings and benefiting for avoiding the oxidation of the interconnector [32].

In addition, Figs. 5(b), 5(e), and 5(h) also show that the micro/nano-particle distribution of MCO-LPPS is the densest and most uniform, followed by MCO-APS and LSM-APS. The cross-section SEM patterns in Figs. 5(c), 5(f), and 5(i) exhibit continuous coating structures of the three samples. This can be explained by the fact that under the function of high temperature plasma, the powders are attached to the surface of SUS430 in a molten state, and fuse with each other, and finally form a

dense and consecutive coating structure. Such melting-induced strong bonding among the powders would result in a high gas tightness of the coating, which is conducive to inhibiting the formation of oxide layer and preventing the diffusion of toxic chromium compounds.

Furthermore, it is also known from Figs. 5(c), 5(f), and 5(i) that the coating thickness of LSM-APS, MCO-APS, and MCO-LPPS is approximately 43, 35, and 35 μm, respectively. The porosity is analyzed by using ImageJ software. Compared to MCO-APS and MCO-LPPS coatings (the porosity being 5.6% and 3.4%, respectively), more pores can be observed locally in the LSM-APS coating (the porosity being 10.1%), suggesting that MCO powders can form a denser coating and the LPPS process can fabricate the lowest porosity coating. As the porosity decreases, the gas barrier performance increases, which can reduce the decay rate of the electrochemical performance of SOCs in long-term operation.

### 3.3 Conductivity and stability of different coatings

The *R* of different rectangular samples was tested by EIS. As Fig. 6(a) shows, the EIS results of SUS430 with LSM-APS, the point the curve intersect with the horizontal coordinate is the *R* of the sample at different temperatures, from which, the corresponding ASR can be calculated using Eq. (1). The ASR of other samples was obtained by the same method. Figure 6(b) compares the ASR of bare SUS430 and SUS430 with LSM-APS and MCO-APS at different temperatures. The MCO-APS exhibits the lowest ASR values of 0.0086, 0.0063, 0.0047, and 0.0033 Ω·cm$^2$ at 650, 700, 750, and 800 °C, respectively.

The ASR of the LSM-APS is higher than that of MCO-APS but lower than that of the bare sample. At 800 °C, for instance, the ASR of the LSM-APS is 0.0100 Ω·cm$^2$, much higher than that of MCO-APS (0.0033 Ω·cm$^2$) and lower than that of the bare sample (0.0340 Ω·cm$^2$). The results illustrate that the oxidation of the bare sample at high temperatures is considerably rapid so that the impedance is significantly higher than that of the coated samples. Although the electronic conductivity of the oxide coatings is lower than that of the interconnector itself, the ASR of the sample with coatings is lower than that of the bare sample because the coatings can inhibit

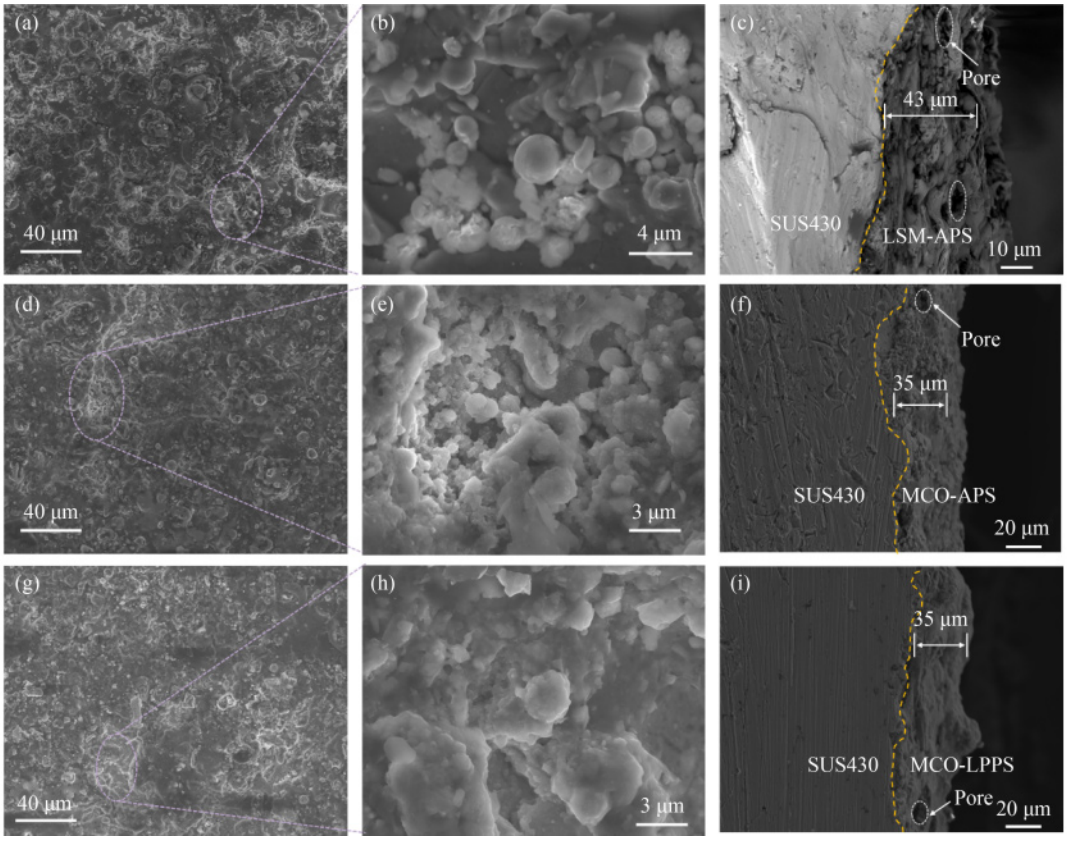


**Fig. 5** Structure and morphology of LSM and MCO coatings.

(a) Surface SEM patterns of SUS430 with LSM-APS coating; (b) locally enlarged images of (a); (c) cross-section SEM patterns of SUS430 with LSM-APS coating; (d) surface SEM patterns of SUS430 with MCO-APS coating; (e) locally enlarged images of (d); (f) cross-section SEM patterns of SUS430 with MCO-APS coating; (g) surface SEM patterns of SUS430 with MCO-LPPS coatings; (h) locally enlarged images of (g); (i) cross-section SEM patterns of SUS430 with MCO-LPPS coating.

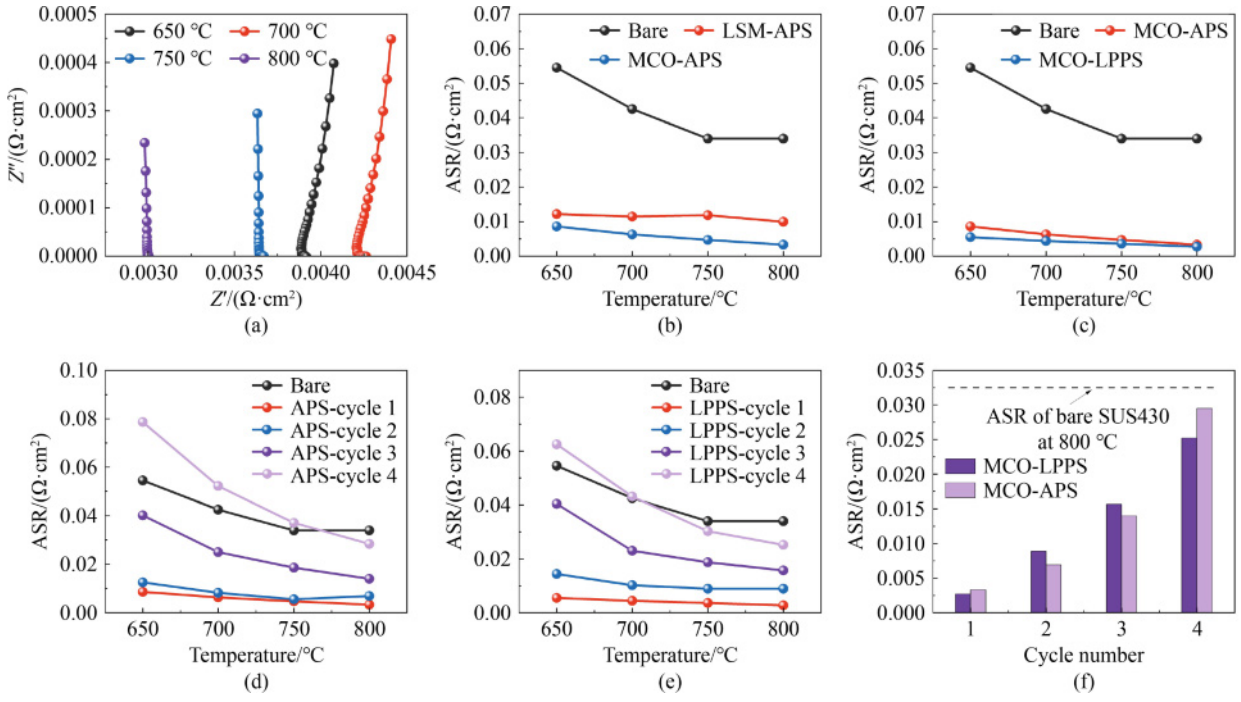


**Fig. 6** ASR test of bare SUS430, LSM, and MCO coating.

(a) EIS test of LSM coating from 600 to 800 °C; (b) ASR comparison of bare SUS430 and SUS430 with LSM-APS and MCO-APS; (c) ASR comparison of MCO-APS and MCO-LPPS; (d, e) rising and cooling cycle test from room temperature to 800 °C of MCO-APS and MCO-LPPS, respectively; (f) ASR comparison of MCO-APS and MCO-LPPS at 800 °C after 4 rising and cooling cycle tests.

the oxidation of the interconnector, which can significantly reduce the electronic conductivity of the interconnector and eventually lead to a rapid performance degradation of the SOC stack. Moreover, Chen et al. [24] fabricated LSM-APS on SUS430. The initial ASR of the sample is similar (0.0150 Ω·cm$^2$) to the result in the present study, and the ASR of the former after oxidation for 300 h in air at 800 °C has barely increased, indicating an excellent long-term oxidation resistance [24]. Furthermore, Fig. 6(b) also indicates that the initial inoxidizability of the MCO coating is better than that of the LSM coating, as the electronic conductivity of the MCO powder is smaller but the ASR of MCO-APS is higher.

The inoxidizability and stability of the rising and cooling cycle test of MCO-APS and MCO-LPPS are analyzed and compared to select a more suitable thermal spraying method for coating preparation. Figure 6(c) shows that the ASR of MCO-LPPS (0.0027 Ω·cm$^2$ at 800 °C) is lower than that of MCO-APS (0.0033 Ω·cm$^2$ at 800 °C) and the bare sample, which means that the initial inoxidizability of MCO-LPPS is stronger than that of MCO-APS. Figures 6(d) and 6(f) show the ASR of MCO-APS and MCO-LPPS for the 4 rising and cooling cycle tests, respectively. The result indicates that at 800 °C, the ASRs of the MCO-APS and MCO-LPPS are still smaller than the initial ASR of the bare sample even after 4 cycle tests, showing the good oxidation resistance and cycle stability of MCO coating.

Moreover, Figs. 6(d) and 6(e) also shows that the ASR of the coated samples increase with the increase of the cycle number, illustrating that the coatings can only delay but cannot completely prevent the oxidation of the interconnector. Furthermore, Fig. 6(f) proves that the ASR of MCO-APS is smaller than that of MCO-LPPS at 800 °C after 2 and 3 cycle tests but the difference is tiny (0.0020 Ω·cm$^2$ after 2 cycle test and 0.0017 Ω·cm$^2$ after 3 cycle test). However, opposite result is observed after 4 cycle and the ASR of MCO-LPPS is 0.0032 Ω·cm$^2$ lower than that of MCO-APS. As a result, it can be concluded that MCO-LPPS has a better oxidation resistance and stability in long-term and frequent rising and cooling cycle operation. The LPPS technology is more suitable for the preparation of the MCO coating for the actual interconnector.

### 3.4 Cr diffusion-inhibited performance

Element distribution on the interface of the two-type sprayed MCO coatings before and after cycle test is analyzed and compared to evaluate the Cr diffusion inhibition performance of the coatings. Fe and Cr are the characteristic elements of SUS430, while Mn and Co are the characteristic elements of MCO. As the EDS patterns demonstrates in Figs. 7(a) and 7(c), the initial MCO-APS and MCO-LPPS samples exhibit a consistent distribution

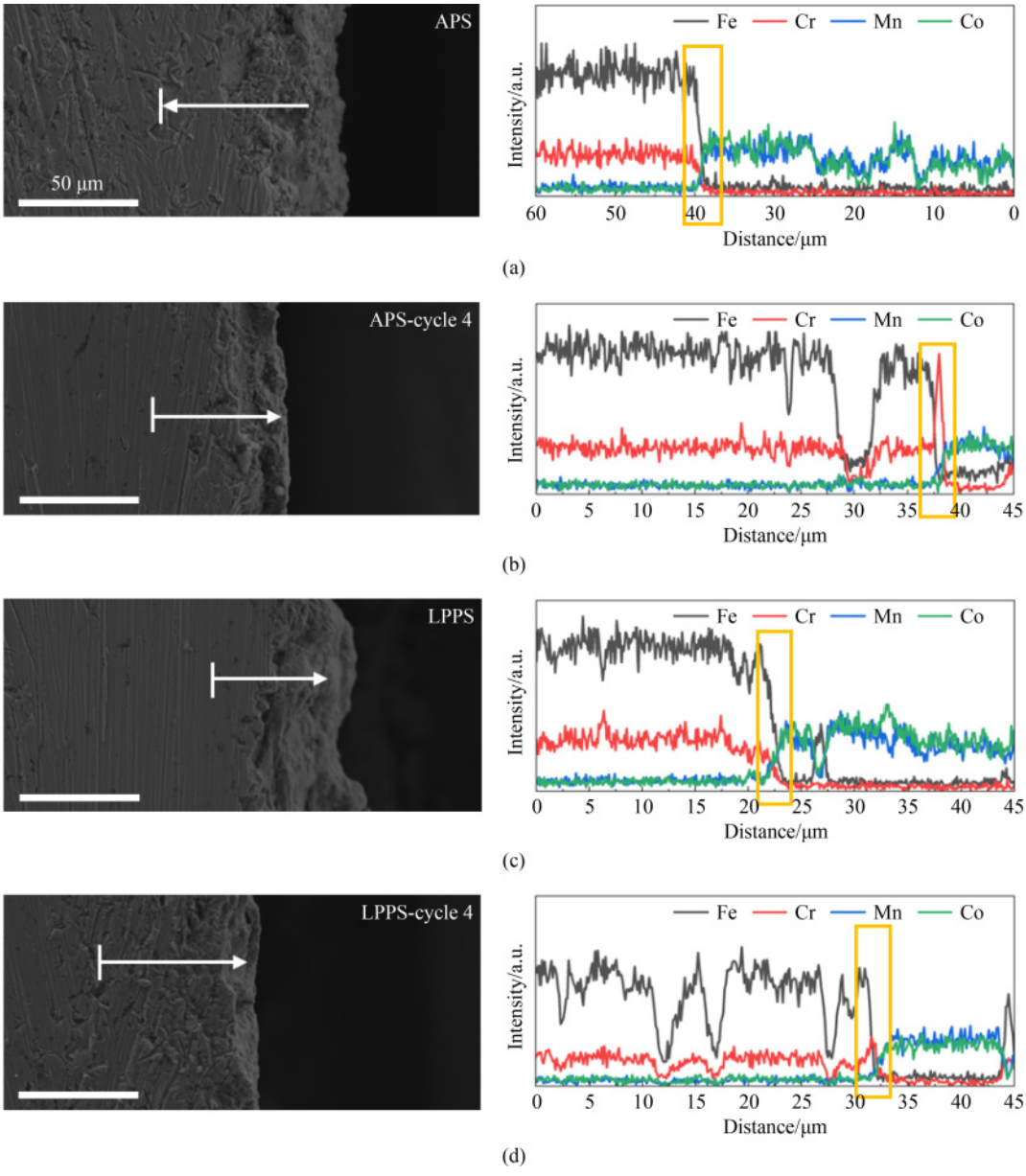


**Fig. 7** EDS element distribution analysis on interface of sprayed coatings.

(a) MCO-APS coating; (b) MCO-APS coating after cycle test; (c) MCO-LPPS coating; (d) MCO-LPPS coating after cycle test (EDS scanning in the direction of the white arrow).

of the characteristic elements near the interface (yellow box area in Fig. 7). Along the direction of the white arrow in Figs. 7(a) and 7(c), Fe and Cr decrease rapidly, while Mn and Co increase significantly at the SUS430/coating interfaces.

After 4 cycle tests, Mn, Co, and Fe exhibit the same distribution pattern as the initial sample, while the element distribution of Cr of the two samples shows a marked difference compared to the initial samples. Cr shows an obvious aggregation and increase at the interface in Figs. 7(b) and 7(d), and the relative content is higher than that of the body phase. The results demonstrate that even if coatings are applied to the surface of SUS430, there still exists the Cr migrating from bulk to interface and forming oxides at the interface during the cycle operations. Additionally, the relative intensity of Cr at the interface in MCO-APS is much higher than that in MCO-LPPS, which means that the MCO-LPPS coating has a better performance than the MCO-APS coating in inhibiting Cr migration and oxide layer growth.

## 4 Conclusions

Interconnector is a critical component for SOC stack

construction. Coating on the interconnector surface is an important method to inhibit the oxidation and Cr migration of the interconnector. In this study, APS and LPPS technology was applied to manufacture LSM and MCO coatings on SOC interconnector surface. In addition, the electrochemical performance and Cr diffusion-inhibited performance of the coatings were analyzed and evaluated. The major conclusions are as follows:

1) The ASRs of MCO-APS and LSM-APS are 0.0010 and 0.0033 $\Omega\cdot cm^2$ at 800 °C, respectively. Although the electrical conductivity of the LSM powder is much higher than that of the MCO powder, MCO-APS has a better electrochemical performance, possibly because MCO-APS can form a denser coating, thereby improving the antioxidant capacity of MCO-APS.

2) The initial ASR of MCO-LLPS is 0.0027 $\Omega\cdot cm^2$ at 800 °C, lower than that of MCO-APS. Moreover, the ASR of MCO-LPPS is 0.0032 $\Omega\cdot cm^2$ lower than that of MCO-APS after 4 cycle operation. Compared to APS, the higher flame temperature and cleaner operating environment of LPPS enable the preparation of denser coatings that exhibit a better oxidation resistance and cycle stability.

3) MCO-LPPS coating has a better performance than MCO-APS coating in inhibiting Cr migration of SUS430. The relative intense of Cr at the interface of SUS430 with MCO-LPPS is lower than that of MCO-APS after 4 rising and cooling cycle operations.

This work provides data support and reference for the performance changes of MCO coatings in frequent start-stop applications in SOC systems. The MCO-LPPS method will be used for the coating preparation of actual interconnectors for the construction of SOC stacks. The electrochemical performance, long-term stability and thermal (cool-down/heat-up) cycles tolerance of the SOC stacks with MCO-LPPS coatings will be tested and evaluated in the SOFC mode and the SOEC mode in the following study. In addition, this work also provides an advanced coating preparation method, which can not only be used for the fabrication of interconnector coatings, but also offer guidance for the coating preparation of key components of other electrochemical devices such as proton exchange membrane fuel cell.

**Competing interests** The authors declare that they have no competing interests.

## References


1. Hauch A, Kungas R, Blennow P, et al. Recent advances in solid oxide cell technology for electrolysis. Science, 2020, 370(6513): eaba6118
2. Zhao C, Li Y, Zhang W, et al. Heterointerface engineering for enhancing the electrochemical performance of solid oxide cells. Energy & Environmental Science, 2020, 13(1): 53–85
3. Zheng Y, Chen Z, Zhang J. Solid oxide electrolysis of $H_2O$ and $CO_2$ to produce hydrogen and low-carbon fuels. Electrochemical Energy Reviews, 2021, 4(3): 508–517
4. Connor P A, Yue X, Savaniu C D, et al. Tailoring SOFC electrode microstructures for improved performance. Advanced Energy Materials, 2018, 8(23): 1800120
5. Jacobs R, Mayeshiba T, Booske J, et al. Material discovery and design principles for stable, high activity perovskite cathodes for solid oxide fuel cells. Advanced Energy Materials, 2018, 8(11): 1702708
6. Duan C, Kee R J, Zhu H, et al. Highly durable, coking and sulfur tolerant, fuel-flexible protonic ceramic fuel cells. Nature, 2018, 557(7704): 217–222
7. Zheng Y, Zhao C, Wu T, et al. Enhanced oxygen reduction kinetics by a porous heterostructured cathode for intermediate temperature solid oxide fuel cells. Energy and AI, 2020, 2: 100027
8. Zheng Y, Zhao C, Li Y, et al. Directly visualizing and exploring local heterointerface with high electro-catalytic activity. Nano Energy, 2020, 78: 105236
9. Cao J, Li Y, Zheng Y, et al. A novel solid oxide electrolysis cell with micro-/nano channel anode for electrolysis at ultra-high current density over 5 $A\cdot cm^{-2}$. Advanced Energy Materials, 2022, 12(28): 2200899
10. Li T, Wang T, Wei T, et al. Robust anode-supported cells with fast oxygen release channels for efficient and stable $CO_2$ electrolysis at ultrahigh current densities. Small, 2021, 17(6): 2007211
11. Zhu J, Zhang W, Li Y, et al. Enhancing $CO_2$ catalytic activation and direct electroreduction on *in-situ* exsolved Fe/$MnO_x$ nanoparticles from $(Pr,Ba)_2Mn_{2-y}Fe_yO_{5+\delta}$ layered perovskites for SOEC cathodes. Applied Catalysis B: Environmental, 2020, 268: 118389
12. Hassan M A, Mamat O B, Mehdi M. Review: Influence of alloy addition and spinel coatings on Cr-based metallic interconnects of solid oxide fuel cells. International Journal of Hydrogen Energy, 2020, 45(46): 25191–25209
13. Sreedhar I, Agarwal B, Goyal P, et al. An overview of degradation in solid oxide fuel cells—Potential clean power sources. Journal of Solid State Electrochemistry, 2020, 24(6): 1239–1270
14. Shaigan N, Qu W, Ivey D G, et al. A review of recent progress in coatings, surface modifications and alloy developments for solid oxide fuel cell ferritic stainless steel interconnects. Journal of Power Sources, 2010, 195(6): 1529–1542
15. Sreedhar I, Agarwal B, Goyal P, et al. Recent advances in material and performance aspects of solid oxide fuel cells. Journal of Electroanalytical Chemistry, 2019, 848: 113315
16. Aznam I, Mah J C W, Muchtar A, et al. A review of key parameters for effective electrophoretic deposition in the fabrication of solid oxide fuel cells. Journal of Zhejiang University. Science A, 2018, 19(11): 811–823
17. Reisert M, Aphale A, Singh P. Solid oxide electrochemical systems: material degradation processes and novel mitigation approaches. Materials, 2018, 11(11): 2169
18. Yang Z, Guo M, Wang N, et al. A short review of cathode

poisoning and corrosion in solid oxide fuel cell. International Journal of Hydrogen Energy, 2017, 42(39): 24948–24959

19. Zhu J H, Ghezel-Ayagh H. Cathode-side electrical contact and contact materials for solid oxide fuel cell stacking: A review. International Journal of Hydrogen Energy, 2017, 42(38): 24278–24300
20. Niu Y, Zhou Y, Lv W, et al. Enhancing oxygen reduction activity and Cr tolerance of solid oxide fuel cell cathodes by a multiphase catalyst coating. Advanced Functional Materials, 2021, 31(19): 2100034
21. Li F, Zhang P, Zhao Y, et al. The preparation and properties of Mn–Co–O spinel coating for SOFC metallic interconnect. International Journal of Hydrogen Energy, 2023, 48(42): 16048–16056
22. Bushuev A, El'Kin O, Tolstobrov I, et al. Development of SOFC interconnects based on industrial steels with oxide coating. Energies, 2023, 16(3): 1237
23. Tomas M, Visibile A, Svensson J E, et al. Novel coatings for protecting solid oxide fuel cell interconnects against the dual-atmosphere effect. International Journal of Hydrogen Energy, 2023, 48(48): 18405–18419
24. Chen J, Lin K, Yang Y, et al. Plasma-sprayed LSM protective coating on metallic interconnect of SOFC. Coatings, 2017, 7(12): 226
25. Jin Y, Hao G, Guo M, et al. Ce-doped $(Mn,Co)_3O_4$ coatings for solid oxide fuel cell interconnect applications. Ceramics International, 2022, 48(23): 34931–34939
26. Jin Y, Sheng J, Hao G, et al. Highly dense $(Mn,Co)_3O_4$ spinel protective coating derived from Mn–Co metal precursors for SOFC interconnect applications. International Journal of Hydrogen Energy, 2022, 47(29): 13960–13968
27. Zhao Y, Zhang S, Su M, et al. *In-situ* formed $CuFe_2O_4$ spinel coating by electroplating method for solid oxide fuel cell interconnect. Chemical Engineering Journal, 2023, 470: 144397
28. Mu J, Geng S, Zhu H, et al. $(Cu, Fe)_3O_4$ spinel coating thermally converted from $Cu–Fe_2O_3$ composite on steel interconnect via electrophoresis-electroplating. High Temperature Corrosion of Materials, 2023, 99(3–4): 267–277
29. Liu D, Geng S, Chen G, et al. $NiO/NiFe_2O_4$ dual-layer coating on pre-oxidized SUS430 steel interconnect. International Journal of Hydrogen Energy, 2022, 47(50): 21462–21471
30. Irankhah R, Raissi B, Maghsoudipour A, et al. $NiFe_2O_4$ spinel protection coating for high-temperature solid oxide fuel cell interconnect application. Journal of Materials Engineering and Performance, 2016, 25(4): 1515–1525
31. Zhao M, Geng S, Chen G, et al. Sputtered $Fe_{1.5}CoNi_{0.5}$ coating: An improved protective coating for SOFC interconnect applications. International Journal of Hydrogen Energy, 2022, 47(22): 11658–11668
32. Yuan K, Zhu J, Dong W, et al. Applying low-pressure plasma spray (LPPS) for coatings in low-temperature SOFC. International Journal of Hydrogen Energy, 2017, 42(34): 22243–22249
33. Lowrance Y N, Azmi M A, Rahman H A, et al. Influence of electrophoretic deposition (EPD) voltage on SOFC interconnect morphology. Key Engineering Materials, 2022, 908: 555–562
34. Norouzi A, Soltanieh M, Rastegari S. An electrophoretic co-deposition of metal oxides followed by *in-situ* copper manganese spinel synthesis on AISI-430 for application in SOFC interconnects. International Journal of Hydrogen Energy, 2022, 47(31): 14346–14360
35. Laicher A, Profitlich T, Schwitzer K. Spray-granulation and drying of granules in a new universal processing unit on the production scale. Die Pharmazeutische Industrie, 1994, 56(3): 276–281